Journal Pre-proof

Honeycomb-Like Nitrogen-Doped Ultramicroporous Biochar for Efficient and Robust CO_2 Capture

Chen Zhang , Duoyong Zhang , Xinqi Zhang , Linrui Chen , Xiaoou Chen , Yongqiang Tian , Liwei Wang

PII: S2667-3258(25)00088-3
DOI: https://doi.org/10.1016/j.fmre.2025.02.005
Reference: FMRE 983

To appear in: *Fundamental Research*

Received date: 24 September 2024
Revised date: 24 January 2025
Accepted date: 7 February 2025

Please cite this article as: Chen Zhang , Duoyong Zhang , Xinqi Zhang , Linrui Chen , Xiaoou Chen , Yongqiang Tian , Liwei Wang , Honeycomb-Like Nitrogen-Doped Ultramicroporous Biochar for Efficient and Robust CO_2 Capture, *Fundamental Research* (2025), doi: https://doi.org/10.1016/j.fmre.2025.02.005

Highlights

- Biochar is synthesized by the one-pot carbonization-activation method from corncob.
- Honeycomb-shaped biochar poses densely packed, nested, and compact ultramicropores.
- Biochar shows graphite state with defects, functional groups, and sorption sites.
- Remarkably high CO_2 sorption capacities reach up to 4.15 mmol/g at 1 bar and 298 K.
- Biochar owns cyclic robustness with an attenuation rate of 13.98% over 20 cycles.

Honeycomb-Like Nitrogen-Doped Ultramicroporous Biochar for Efficient and Robust CO_2 Capture

Chen Zhang[a,b], Duoyong Zhang[a,b], Xinqi Zhang[b,c], Linrui Chen[a,b], Xiaoou Chen[a,b], Yongqiang Tian[d], Liwei Wang[a,b,*]

[a] *Institute of Refrigeration and Cryogenics, Key Laboratory of Power Machinery and Engineering of MOE, School of Mechanical Engineering, Shanghai Jiao Tong University, Shanghai 200240, China.*

[b] *Shanghai Non-Carbon Energy Conversion and Utilization Institute, Shanghai 200240, China*

[c] *China-UK Low Carbon College, Shanghai Jiao Tong University, Shanghai 201306, China*

[d] *College of Smart Energy, Shanghai Jiao Tong University, Shanghai 200240, China*

** Corresponding author: lwwang@sjtu.edu.cn (L.W. Wang).*

ABSTRACT

Honeycomb-like nitrogen-doped ultramicroporous biochar for CO_2 capture is synthesized through various methods utilizing biomass, urea, and KOH as raw materials, nitridation agent, and porogen, respectively. The resulting materials meticulously undergo comprehensive characterization, revealing densely packed ultramicropores arranged in honeycomb-like patterns. The biochar predominantly exists in a graphite state of carbon with sufficient defects and abundant functional groups, along with a high nitrogen content, thereby providing numerous CO_2 sorption sites. High CO_2 sorption capacities are observed of 4.15 mmol/g (at 1 bar and 298 K) and 5.45 mmol/g (at 1 bar and 273 K) with sorption heat around 23 kJ/mol. The Sips model fitting displays satisfactory results at 298 K, indicating a maximum sorption capacity around 5.45 mmol/g, with regression correlation coefficients exceeding 0.9942. The sorption selectivity between CO_2 and N_2 is notably influenced by the surface nitrogen content present in the materials. These sorbents exhibit exceptional cyclic robustness during vacuum pressure swing cycles, with an attenuation rate as low as 13.98% over 20 cycles. The abundant availability and cost-effectiveness of biomass, combined with a straightforward synthesis procedure and excellent CO_2 sorption performance, position honeycomb-like N-doped ultramicroporous biochar synthesized through the one-pot carbonization-activation method as promising candidates for CO_2 capture applications.

Keywords: ultramicropore; biomass; nitrogen-doped; carbon dioxide capture; biochar

1. Introduction

The imperative to address climate change, exacerbated by escalating carbon dioxide (CO_2) emissions, has propelled sorption-based technologies for CO_2 capture to the forefront of mitigation strategies [1-4]. Yet, the efficiency of CO_2 capture remains tethered to the sorption characteristics of current sorbents [5-7]. Encouragingly, a diverse array of sorbents has undergone exploration for CO_2 capture, namely alkaline ceramics [8-10], metal oxides [11, 12], alkali metal carbonates [13, 14], and notably, porous materials [15, 16]. Porous materials have garnered significant prominence due to their inherent attributes, including abundant sorption sites, tunable microstructure and microenvironment, and rapid sorption kinetics [17, 18]. The expansive landscape of porous materials for CO_2 capture spans diverse categories, namely porous carbons [19, 20], zeolites [21, 22], metal-organic frameworks [23, 24], porous organic frameworks [25], layered double hydroxides [26], mesoporous silicas [27], γ-alumina [28], and polymers [29]. Within this category, porous carbon derived from biomass sources, termed biochar, has emerged as particular allure for CO_2 capture, with its appeal lying in its remarkable durability, cost-effectiveness, facile synthesis methods, and a broad spectrum of customizable sizes ranging from nanometers to micrometers, but its comparatively lower sorption capacity constrains as compelling candidates [30-34].

Fortunately, the fortuitous infusion of nitrogen into microporous biochar emerges as a transformative strategy, dramatically amplifying the sorption efficacy of microporous biochar [35]. This enhancement is attributed to the large electric quadrupole moments possessed by CO_2 molecules, primarily associated with the robust dipolar nature of C=O bonds [36]. These molecular nuances underscore a heightened affinity toward N-doped porous biochar compared to its regular counterparts [37]. In a pioneering exploration, Adio et al. employed density functional theory calculations to delve into the impact of nitrogen doping on sorption performance [38]. A meticulous comparison of sorption capacities, conducted at 25°C and 1 atm, between pristine and nitrogen-doped biochar derived from sugarcane bagasse revealed a noteworthy advancement that N-doped boichar exhibited a substantial improvement, registering a sorption capacity of 3.34 mmol/g, in stark contrast to the modest 1.51 mmol/g displayed by their pristine counterparts. This empirical evidence underscores the pivotal role of nitrogen incorporation in elevating the sorption prowess of biochar, marking a promising stride toward enhancing the efficiency of CO_2 capture technologies.

Two primary synthetic pathways for N-doped biochar, the direct carbonization method and the hydrothermal method, present distinctive approaches with their own merits and challenges. The direct carbonization method, a robust technique, involves nitridation and carbonization reactions followed by activation processes. For instance, waste walnut shells underwent treatment with H_3PO_4, subsequently nitrogen-doped via urea at 350°C for 2 hours, achieving a nitrogen content of 2.21% [39]. Activation with KOH, K_2CO_3, or $ZnCl_2$ yielded nitrogen-doped biochar boasting a remarkable specific surface area of 2354 m^2/g, exhibiting a peak sorption capacity of 3.08 mmol/g

at 25°C and 1 bar. Analogously, water caltrop shells were nitrogenized via melamine, carbonized at 550°C for 2 hours, and activated with KOH, yielding N-doped biochar with a noteworthy 8.48% nitrogen content [40]. This synergistic approach resulted in a remarkable sorption capacity of 4.22 mmol/g at 25°C and 1 bar, attributed to the interplay between nitrogen content and narrow microporous volumes. Lotus leaves-derived biochar prepared through the same method displayed a commendable maximum sorption capacity of approximately 3.87 mmol/g under equivalent conditions [41]. On the other hand, the hydrothermal method offers an alternative, substituting nitridation and carbonization with a hydrothermal reaction at lower temperatures, which facilitates the retention of N-containing functional groups for improving sorption performance. Yue et al. harnessed this method at 180°C for 12 h to prepare N-doped biochar using rotten strawberries as carbon and nitrogen precursors [42]. This biochar manifested a notable sorption capacity of 4.49 mmol/g for CO_2 at 25°C and 1 bar, attributed to the uniform distribution of nitrogen atoms within the porous biochar. Another instance involved a hydrothermal reaction with d-glucose and urea, resulting in N-enriched porous biochar with a sorption capacity of 4.26 mmol/g at 25°C and 1 bar, accompanied by rapid reaction kinetics [43].

As of now, the integration of nitrogen into microporous carbons derived from biomass sources emerges as a great promising avenue for enhancing CO_2 sorption capabilities. However, the exploration of both direct carbonization method and hydrothermal method has revealed a landscape of distinct promise and limitations. Notably, it is important to acknowledge the inherent complexity of their two-step fabrication processes, which leads to substantial substance volatilization and reduced yields. Striking a balance between efficiency and simplicity remains a crucial consideration in the pursuit of optimal nitrogen-doped biochar for CO_2 capture applications. Hence, further research is imperative to compare and optimize these approaches, paving the way for the development of efficient and practical sorbents tailored for CO_2 capture.

Herein, we embark on a pioneering comparative investigation to systematically evaluate various synthetic methods, namely direct carbonization method, hydrothermal method, and one-pot carbonization-activation method, for the fabrication of honeycomb-like N-doped ultramicroporous biochar derived from biomass. These methods are explored to discern their effectiveness in crafting the unique honeycomb-like microstructure while enhancing material properties for CO_2 capture. The research unfolds with a meticulous analysis of the physical and chemical properties of the samples, employing detailed characterization techniques. Experimental tests follow suit, probing the sorption capacities, sorption heat, sorption selectivity, and cyclic robustness of the samples, while isotherm reconstruction is employed to model and unravel their sorption behavior. By holistically comparing the outcomes of these synthetic strategies, this work identifies the optimal pathway for synthesizing high-performance, cost-effective biochar tailored for selective and durable CO_2 capture, underscoring the potential of biochar as sustainable solutions for addressing carbon emissions.

2. Material and methods

2.1. Materials

The chemicals employed in the experiment, namely KOH and HCl sourced from Sinopharm Chemical Reagent, and urea obtained from General-reagent, are utilized in their original state without undergoing any supplementary purification processes. The gases, including Helium, CO_2, and N_2, are procured from Liquefied Air (Shanghai) Compressed Gas. The biomass, chiefly waste corncobs, serving as biomass precursors for the synthesis of honeycomb-like N-doped ultramicroporous biochar, is responsibly collected from Xinjiang province, China. The biomass undergoes a meticulous pretreat process to be prepared for experimentation. Initially, they are subjected to a drying period at 110°C for 24 hours under vacuum conditions, ensuring the removal of moisture. Subsequently, the dried biomass is ground into powders, with particle sizes meticulously reduced to dimensions smaller than 100 mesh. This preparation ensures the uniformity and consistency of the biomass precursor, laying a solid foundation for the subsequent stages of the experimental process.

2.2. Fabrications of honeycomb-like N-doped ultramicroporous biochar

The synthesis of honeycomb-like N-doped ultramicroporous biochar involves three distinct methods with both common and preferred activation temperatures and raw material ratios [44], each meticulously designed to achieve optimal results:

Direct carbonization method: 10 g of biomass and 3 g of urea are subjected to heating in a muffle furnace at 500°C for 2 h. The resulting powders, called as DNdC, are impregnated with a KOH solution at a mass ratio of approximately 1:1, followed by activating in a tube furnace at 700°C for 1 h with a heating rate of 5°C/min in a N_2 flow. The activated DNdC is washed with HCl until the pH reaches around 7.0, yielding DNdCA after drying at 85°C under vacuum. The yield for DNdC and DNdCA is reported as 22.15% and 13.87%, respectively.

Hydrothermal method: 10 g of biomass and 10 g of urea are dissolved into 110 mL of deionized water, undergoing a hydrothermal reaction at 180°C for 12 h with stirring at 600 rpm. The product, termed HNdC, is collected and washed with deionized water, sieved through a 200-mesh sieve, and dried at 85°C under vacuum overnight. The HNdC powders are then impregnated with a KOH solution at a mass ratio of approximately 1:1, followed by activation in a tube furnace at 700°C for 1 h with a heating rate of 5°C/min in N_2 flow. The activated HNdC is washed with HCl until the pH reaches around 7.0, yielding HNdCA after drying at 85°C under vacuum. The yield for HNdC and HNdCA is reported as 58.70% and 25.22%, respectively.

One-pot carbonization-activation method: 10 g of biomass, 10 g of KOH, and 3 g urea are uniformly mixed, afterward undergone carbonization at 700°C for 1 h with a heating rate of 5°C/min under N_2 atmosphere. Subsequently, washing with HCl and deionized water removes KOH, and the resulting mixture is dried at 85°C under vacuum overnight to obtain PNdCA. The yield for PNdCA is approximately 20.50%.

The observed differences in yields among the activated samples can primarily be attributed to variations in the carbonization conditions. For DNdCA, the carbonization process is conducted at 500°C for 2 hours, conditions that likely lead to greater material loss due to the prolonged exposure to high temperature, which facilitates the decomposition and volatilization of organic components. In contrast, HNdCA is synthesized via a hydrothermal method, which operates at a comparatively lower reaction temperature, thereby retaining more of the material. Similarly, PNdCA, prepared using a one-pot carbonization-activation method, involves a lower temperature and shorter heating time, further minimizing material loss. These distinctions in processing conditions contribute to the higher yields observed for HNdCA and PNdCA relative to DNdCA.

2.3. Characterizations

The microcosmic morphologies of the samples are meticulously examined through scanning electron microscopy (SEM) utilizing a Regulus 8100 Japan Hitachi performing at 5.0 kV. Nitrogen sorption/desorption isotherms are acquired at 77 K on a TriStar II 3020 Micromeritics America to delve into the porosity characteristics. The Brunnauer-Emmett-Teller (BET) method is applied to compute the specific surface area (S_{BET}), employing the isothermal sorption data within the relative pressure range of 0.005 to 0.1, a region where N_2 molecules are primarily sorbed as a single monolayer on the surface of the material. By focusing on this range, the BET method provides a reliable estimate of the specific surface area. Additionally, the micropore area (S_{mic}) and the micropore volume (V_{mic}) are determined via the t-plot method, while the total pore volume (V_t) is gauged based on the sorption capacity of N_2 sorbed at a relative pressure of 0.99. Moreover, CO_2 sorption/desorption isotherms are investigated at 273.15 K on a TriStar II Plus Micromeritics America for a more comprehensive understanding of the ultramicroporous structure (<1 nm). This analysis involves assessing the ultramicropore volume (V_{S1}), specific surface area in ultramicropores (S_{S1}), specific surface area in pores larger than 1 nm (S_{L1}), and ultramicroporous porosity distribution via the density functional theory model. The median pore diameter (d_a) is calculated through the Horvath-Kawazoe method. Thermal robustness is evaluated through thermogravimetry coupled with differential scanning calorimetry (TG-DSC) with a TGA/DSC 3+ Mettler Toledo Switzerland. Crystallinity is assessed via X-ray diffraction (XRD) and Raman spectra conducted in a SmartLab (3 KW) Rigaku Japan and a LabRAM HR Evolution HORIBA France (λ = 532 nm), respectively. Surface properties of the samples are explored using Fourier-transform infrared spectroscopy (FT-IR) with a Nicolet iS50 FT-IR Thermo American. The surface and bulk elemental composition is analyzed employing X-ray photoelectron spectroscopy (XPS) and element analysis (EA) with a ESCELAB 250XI Thermo America and a Vario EL Elementar Germany, respectively. This multifaceted analytical approach ensures a comprehensive exploration of the structural, thermal, and surface characteristics of the synthesized samples.

2.4. Sorption measurements

The sorption characteristics of CO_2 and N_2 are determined by a high- and low-pressure adsorption analyzer (H-Sorb 2600TL, Ultmetrics, China) at 273 K and 298 K with a pressure range of 0-1.00 bar. The samples undergo a pretreatment at 353 K for 3 hours, employing a heating rate of 8°C/min, to ensure accurate measurements by completely desorbing any gases trapped within the samples. The sorption heat of the samples is calculated via the Clausius-Clapeyron equation (Equation 1 [45]), utilizing the experimental sorption isotherms at 273 K and 298 K. Additionally, sorption selectivity ($S_{C/N}$) based on ideal adsorption solution theory is quantified through Equation 2, offering insights into the relative affinity of the sorbent for CO_2 versus N_2. Furthermore, various isothermal models (Equation 3-7), including the Langmuir model, Freundlich model, Toth model, Sips model, and Temkin model, are applied to reconstruct the sorption isotherms. This fitting process yields critical parameters such as the maximum sorption capacity, equilibrium constant, and sorption energy, providing a comprehensive understanding on the sorption behavior of the samples. The same equipment is employed under identical pretreatment conditions for 20 cycles of vacuum pressure swing sorption to assess the sorption cyclic robustness. This iterative testing allows the calculation of the attenuation of sorption capacity, offering valuable insights into the long-term stability and reliability of the sorption materials under realistic operating conditions.

$$Q = \left[RT_1T_2 \ln\left(p_1 / p_2 \right) \right] / \left(T_1 - T_2 \right) \quad (1)$$

$$S_{C/N} = \left(x_{CO_2} / x_{N_2} \right) / \left(y_{CO_2} / y_{N_2} \right) \quad (2)$$

Langmuir model: $q = q_m Bp / (1 + Bp)$ (3)

Freundlich model: $q = Kp^{1/n}$ (4)

Toth model: $q = q_m Bp \Big/ \left[1 + \left(Bp \right)^n \right]^{1/n}$ (5)

Sips model: $q = q_m Bp^n / \left(1 + Bp^n \right)$ (6)

Temkin model: $q = B \ln(Ap)$ (7)

where x_{CO2} and x_{N2} represent the molar fractions of CO_2 and N_2 in the samples, respectively, and y_{CO2} and y_{N2} are the molar fractions of CO_2 and N_2 in the feed gas, individually, Q, R, T, p, and q represent sorption heat, molar gas constant, temperature, pressure, and sorption capacity, separately, while A, B, K, and n are fit parameters.

Dynamic breakthrough experiments are performed under mixed gas conditions (15% CO_2 and 85% N_2) at 298 K and 1 bar to evaluate the practical gas separation capability of the sorbents. The tests utilized a stainless steel column (4 mm inner diameter, 100 mm length) load with samples. A purge gas flow rate of 5 sccm is maintained during the experiments. Prior to testing, the sample is regenerated by heating at 353 K for 2 h with N_2 as the carrier gas. The composition of the effluent

gas was continuously monitored by an online mass spectrometer, providing real-time insights into the gas separation performance of the sorbent materials.

2.5. Theoretical calculation details

To evaluate the impact of N doping on CO_2 sorption, the synthetized honeycomb-like N-doped ultramicroporous biochar is simplified into a graphene layer cluster model and subjected to density functional theory (DFT) calculations via Gaussian 16 code package [46]. After geometric optimization of the cluster model with B3LYP functional [47] and 6-311++G(d,p) basis set, the sorption of a single CO_2 molecule is investigated employing M062X functional [48] and def2TZVP basis set [49, 50], incorporating Grimme's D3 dispersion force correction [51]. The analyses encompass the electrostatic potential distribution, charge distribution, and microstructural modifications of the cluster upon CO_2 sorption. Visualizations generated by VMD 1.9.3 [52] and Multiwfn 3.8 [53] software packages elucidate the sorption mechanisms, underscoring the pivotal role of N doping in boosting the CO_2 capture capabilities of the biochar material.

3. Results and discussion

3.1. Surface porous morphology and thermal robustness

Figure 1 illustrates the microscopic morphologies of the investigated samples observed through SEM. The pristine biomass displays a typical biomass surface morphology, characterized by irregular large block particles with a relatively small number of visible pores (Figure 1a). There is still a lack of obvious pores compared to the pristine biomass, following N-doping operations via urea in both the direct carbonization method (Figure 1b) and the hydrothermal method (Figure 1c). In contrast, the introduction of KOH in the activation step proves to be effective in inducing the growth and expansion of ultramicropores in the activated N-doped ultramicroporous biochar. The SEM images of HNdCA, DNdCA, and PNdCA (Figure 1d-1f, respectively) reveal the significant development of microstructures. Notably, PNdCA exhibits densely packed ultramicropores arranged in a honeycomb-like pattern, forming a nested and compact pore morphology. This intricate pore structure suggests enhanced surface area and porosity, manifesting the effectiveness of the activation step, particularly in the case of one-pot carbonization-activation method.

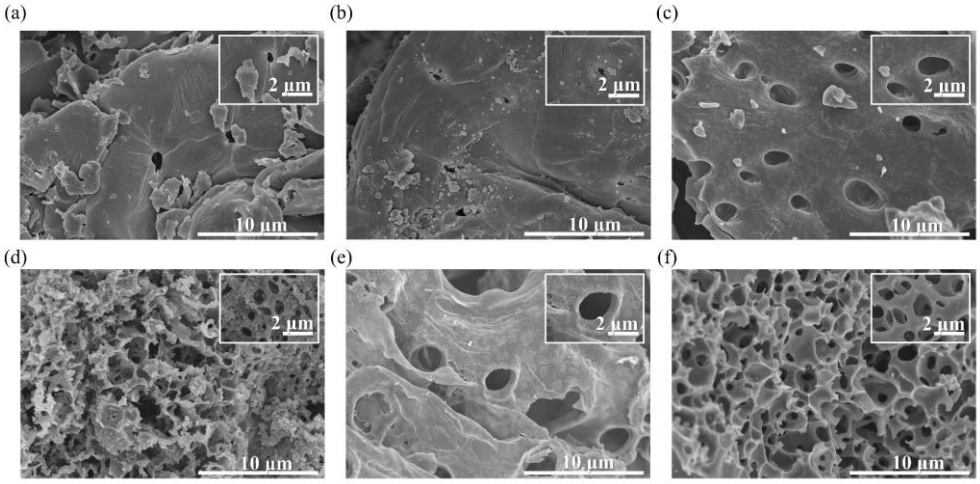

Figure 1. SEM images of (a) biomass, (b) HNdC, (c) DNdC, (d) HNdCA, (e) DNdCA, (f) PNdCA.

Figure 2a presents the N_2 sorption/desorption isotherms, offering insights into the intricate pore structures of the investigated honeycomb-like N-doped ultramicroporous biochar. The isotherms of PNdCA and DNdCA exhibit classical type I graphs, identified by International Union of Pure and Applied Chemistry (IUPAC), indicative of the presence of abundant well-developed micropores. However, the isotherm of HNdCA displays a type II graph, suggesting a coexistence of micropores and macropores (> 100 Å, Figure 2b). In contrast, the biomass, HNdC, and DNdC feature type III isotherms, highlighting weak sorption behaviors and the absence of significant microporosity. Therefore, the micropores are prevalent in HNdCA, DNdCA, and PNdCA, while HNdCA primarily features mesopores, as evidenced by the increase in sorption capacity at P/P_0 > 0.1 (Figure 2a) and the porosity distribution of the N-doped microporous biochar (Figure 2b). Additionally, the CO_2 sorption/desorption isotherms (Figure 2c) are conducted to analyze the detailed ultramicroporous porosity distribution of activated samples, namely HNdCA, DNdCA, and PNdCA, within the range of 2 Å to 10 Å. These isotherms feature typical type I sorption behavior. Figure 2d further reveals that most pores in these samples are in the range of 3 Å to 6 Å, with PNdCA demonstrating a superior ultramicropores structure contrasted to both DNdCA and HNdCA.

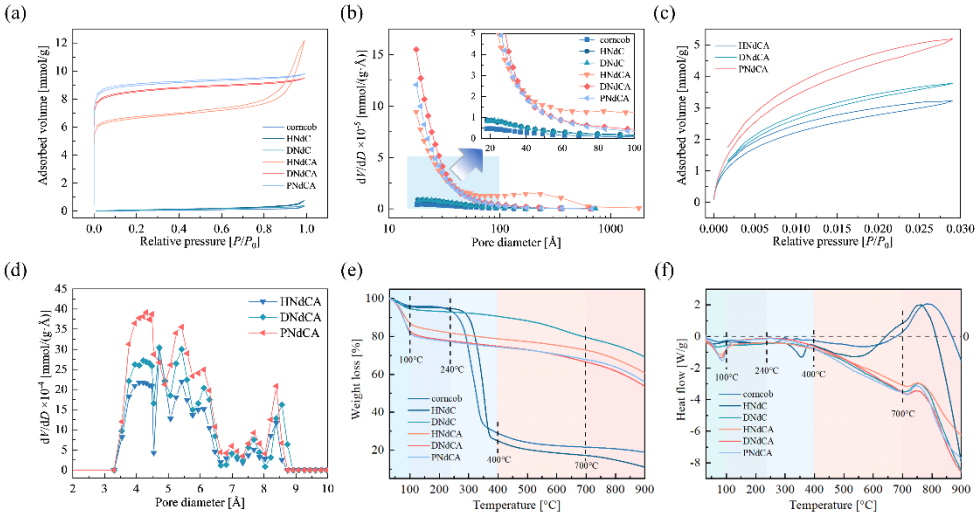

Figure 2. Porous properties and thermal robustness of the samples: (a) N_2 sorption/desorption isotherms, (b) porosity distributions of the samples, (c) CO_2 sorption/desorption isotherms, (d) ultramicroporous porosity distributions of the samples, (e) TGA, (f) DSC.

Table 1 provides a comprehensive summary of the specific surface area and total pore volume of the investigated samples, as determined through the aforementioned sorption isotherms. The pristine biomass exhibits a specific surface area of only 5.62 m^2/g and a total pore volume of 0.0116 cm^3/g, indicating a lack of significant porosity. N-doping via the direct carbonization method and the hydrothermal method results in a slight enhancement in specific surface area and total pore volume, but there is still no substantial growth in micropores. However, the activation reaction proves pivotal in pore growth, particularly in ultramicropores, in the honeycomb-like N-doped ultramicroporous biochar. Notably, the honeycomb-like N-doped ultramicroporous biochar prepared via the one-pot carbonization-activation method (PNdCA) boasts the largest specific surface area at approximately 646.86 m^2/g, with 565.99 m^2/g attributed to micropores. The total pore volume of PNdCA also experiences a significant improvement, reaching 0.3404 cm^3/g. Given the pronounced impact of ultramicropores with diameters smaller than 10 Å on CO_2 sorption [54], the S_{S1} and V_{S1} of PNdCA stand out at 23.05% - 49.12% and 23.93% - 55.20%, respectively, surpassing other activated samples. Additionally, the median pore diameters of HNdCA, DNdCA, and PNdCA are listed as 3.57 Å, 3.56 Å, and 3.70 Å. These results collectively underscore a substantial enhancement in specific surface area, total pore volume, and ultramicroporosity for activated samples compared to the pristine biomass.

Table 1: Porous properties of N-doped ultramicroporous biochar and its precursors

Materials	S_{BET} [m^2/g]$^{a)}$	S_{mic} [m^2/g]$^{a)}$	S_{S1} [m^2/g]$^{b)}$	S_{L1} [m^2/g]$^{b)}$	V_t [cm^3/g]$^{a)}$	V_{mic} [cm^3/g]$^{a)}$	V_{S1} [cm^3/g]$^{b)}$	d_a [Å]$^{b)}$

Biomass	5.62	0.00	/	/	0.0116	0.0000	/	/
HNdC	9.54	0.00	/	/	0.0266	0.0000	/	/
DNdC	8.10	0.00	/	/	0.0140	0.0000	/	/
HNdCA	481.23	388.83	405.17	178.10	0.4235	0.1895	0.1076	3.57
DNdCA	615.90	514.22	491.00	189.83	0.3299	0.2506	0.1347	3.56
PNdCA	646.86	565.99	604.19	342.82	0.3404	0.2757	0.1670	3.70

[a] Measuring by N_2 adsorption isotherms at 77 K, [b] Conducted by CO_2 adsorption isotherms at 273.15 K.

The thermal robustness of the samples is assessed through TGA, as depicted in Figure 2e and Figure 2f, within the temperature range of 50-900°C. An endothermic peak is consistently observed in all samples below 100°C, attributed to the desorption of captured gas molecules from the ultramicropores or the surface. Both the biomass and HNdC exhibit a rapid decomposition of cellulose, featuring endothermic peaks in the 240-400°C range, resulting in a total weight decrease to approximately 20%. Volatile substances in the samples are subsequently released at temperatures exceeding 700°C, accompanied by slightly exothermic processes and weight loss. In summary, the carbonized and activated samples demonstrate excellent thermal robustness below 700°C. This observation indicates their potential for stable and continuous CO_2 capture, as they can withstand higher temperatures without significant degradation or pore collapse. The TGA results affirm the suitability of the materials for applications requiring thermal stability in the context of CO_2 sorption.

3.2. Phase structure

Figure 3a depicts the XRD profiles of the samples, and the crystallinity indexes (CrI) are calculated using the Segal empirical method [55]. The CrI is determined by comparing the maximum intensity of the (002) lattice reflection of the cellulose crystallographic form I (I_{002}) at 2θ = 22° and the diffraction of the amorphous material (I_{am}) at 2θ = 16°, as described in Equation 8.

$$\mathrm{CrI} = \left(I_{002} - I_{\mathrm{am}}\right)/I_{002} \times 100\% \quad (8)$$

While the biomass and HNdC exhibit similar diffraction peaks at 16° and 22°, representing the crystal lattice type I structure of native cellulose [56, 57], the CrI of HNdC is amplified by 36.25% contrasted to that of biomass. This increase is attributed to the hydrothermal treatment, which removes amorphous solid impurities and enlarges the specific surface area and total pore volume. Additionally, two diffraction peaks at 23.5° and 43° are observed in the carbonized and activated samples, namely DNdC, HNdCA, DNdCA, and PNdCA, ascribing to the (002) and (100) planes of graphene, separately [58]. The presence of these peaks indicates the formation of graphitic structures in the samples after carbonization or activation.

Furthermore, the amorphous characteristics are examined through the Raman spectra, as illustrated in Figure 3b. In agreement with the XRD results, both biomass and HNdC display similar features without distinct bands. However, the carbonized or activated samples exhibit two prominent signals at approximately 1350 cm^{-1} and 1580 cm^{-1}, corresponding to the defect bands (D-band) [59] and graphitic bands (G-band) [60], individually. The D-band, originating from lattice defects and primarily attributed to the A_{1g} mode of defective carbons, plays a significant role in shaping the microstructure and microenvironment. Conversely, the G-band corresponds to the E_{2g} mode for sp^2-hybridized graphitic carbons, enhancing heat conductivity. Given the necessity of a balanced optimization between microstructure, microenvironment, and heat transfer for effective sorption processes, achieving an optimal I_D/I_G ratio of approximately 1 is highly desirable [61]. This balance enhances the CO_2 capture performance by promoting efficient interactions between the sorbent and CO_2 molecules. The distinct signals in the Raman spectra provide valuable insights into the structural properties of the carbonized or activated samples, indicating the presence of defect and graphitic structures crucial for their enhanced performance.

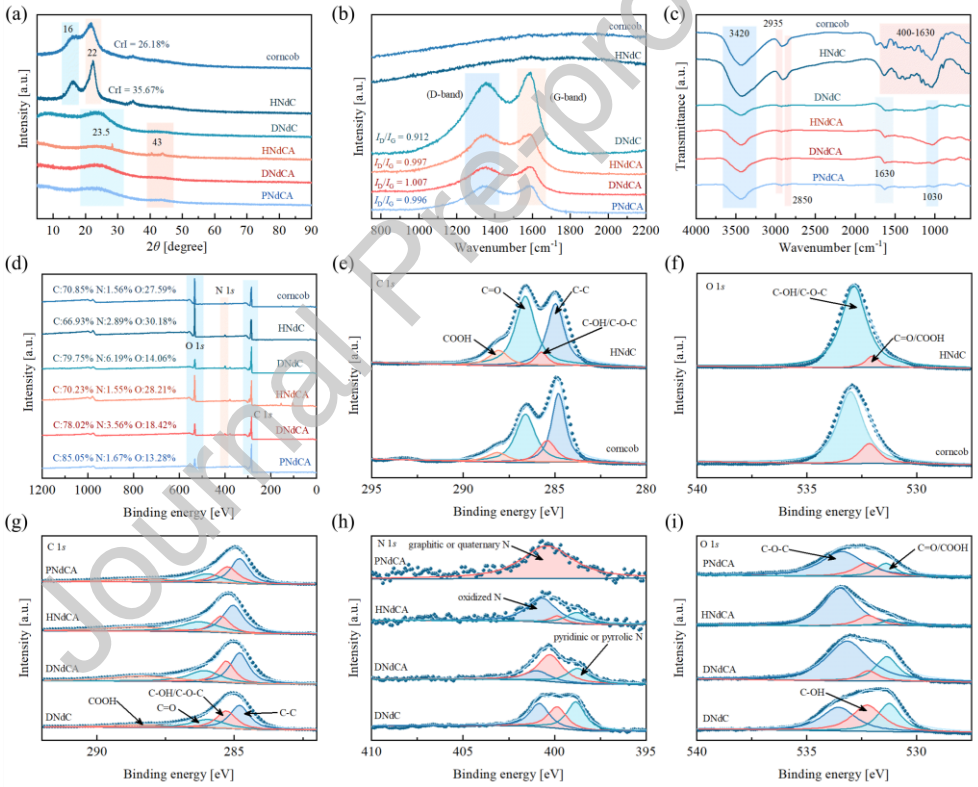

Figure 3. Phase structure characterization profiles of the samples: (a) XRD, (b) Raman, (c) FT-IR, (d) XPS spectra for survey scans, (e) C 1*s* of biomass and HNdC, (f) O 1*s* of biomass and HNdC, (g) C 1*s* of carbonized and activated samples, (h) N 1*s* of carbonized and activated samples, (i) O 1*s* of carbonized and activated samples.

The surface functionalities of the samples are characterized by FT-IR spectroscopy, as depicted in Figure 3c. The broad band observed around 3420 cm^{-1} is commonly attributed to the stretching vibrations of surface N-H and/or O-H groups

[62]. Peaks at 2935 cm^{-1} and 2850 cm^{-1} correspond to the -CH_2- bond, which is abundant in biomass and HNdC. However, these peaks are scarce in the carbonized or activated samples, as most of these bonds are volatilized or broken during carbonization or activation heating above 200°C. The stretching vibrations of C=N and C-N bonds are reflected by peaks at 1630 cm^{-1} and 1030 cm^{-1}, respectively. Remarkably, the hydrothermal treatment preserves numerous surface functional groups of the biomass, as evidenced by the similarity in absorption peaks between HNdC and biomass in the spectral range from 1630 cm^{-1} to 400 cm^{-1}.

XPS is performed to gain further insights into the chemical structures and syntactic arrangement of the honeycomb-like N-doped ultramicroporous biochar and its precursors. The survey scans (Figure 3d) confirm the presence of C, N, and O elements on the surface of samples. This indicates that the N-doping process and carbonization procedure enrich the contents of N and C elements while release byproducts with O elements. However, the hydrothermal reaction maintains abundant O elements and introduces N atoms while relatively reduce C content during the generation biochar. Furthermore, the element analysis on the bulk phase of the honeycomb-like N-doped ultramicroporous biochar (Figure S1) highlights the PNdCA has the highest ratio between surface nitrogen content and bulk nitrogen content, approximately 1.50, among activated samples. This suggests that PNdCA exhibits a relatively higher concentration of surface N compared to its bulk nitrogen content, indicating a more efficient N-doping process and potentially contributing to its superior performance in CO_2 capture applications. The fitted curves and Gaussian deconvoluted peaks of C 1*s*, N 1*s*, and O 1*s* spectra are illustrated in Figure 3e-3i. In Figure 3e and Figure 3f, the observed bands at approximately 284.8 eV (C-C), 285.4 eV (C-OH or C-O-C), 286.6 eV (C=O), 288.1 eV (COOH), 532.2 eV (C=O or COOH), and 533.0 eV (C-O-C or C-OH) can be attributed to cellulose [63, 64]. This further supports that the hydrothermal reaction preserves hydroxyl groups as active sites for sorption. The characteristic peaks of C-C in Figure 3g demonstrate larger area ratios compared to those in Figure 3e, suggesting that stable C-C bonds become the dominant form of carbon in the samples due to the release of volatile substances during carbonization or activation procedures. Moreover, the high-resolution N 1*s* spectrum in Figure 3h exhibits three distinct peaks at 398.8 eV (pyridinic or pyrrolic N), 399.9 eV (graphitic or quaternary N), and 400.8 eV (oxidized N) [65]. The activated honeycomb-like N-doped ultramicroporous biochar, with its main nitrogen presence in the form of pyridinic or pyrrolic N (398.8 eV) and graphitic or quaternary N (399.9 eV), exhibits a higher capacity for trapping CO_2 molecules due to the abundance of sorption sites and excellent electronegativity, while the oxidized N (400.8 eV) in biochar hinders capture performance. Furthermore, the deconvoluted peaks in the O 1*s* spectrum of the carbonized and activated samples (Figure 3i) can be identified as 531.24 eV (C=O or COOH), 532.24 eV (C-OH), and 533.54 eV (C-O-C) [66].

The production of honeycomb-like N-doped ultramicroporous biochar has been successfully achieved, leading to the carbon primarily existing in a graphite state with noticeable defects as sorption sites. A comprehensive analysis, involving XRD,

Raman spectroscopy, FT-IR, XPS, and EA, collectively confirms the presence of abundant functional groups and numerous CO_2 sorption sites within the biochar structure.

3.3. CO_2 sorption performance

Figure 4a presents the sorption isotherms of CO_2 for honeycomb-like N-doped ultramicroporous biochar and its precursors, manifesting an increase in sorption capacities as CO_2 partial pressure enhances. The sorption capacity of PNdCA at 298 K is approximately 4.15 mmol/g, significantly surpassing the capacity of biomass, which can only trap 0.07 mmol/g CO_2 under the same condition. Moreover, the sorption capacities of DNdCA (3.56 mmol/g) and HNdCA (3.19 mmol/g) also exhibit substantial enhancements contrasted with their precursors (0.01 mmol/g for HNdC and 1.26 mmol/g for DNdC). Therefore, this correlation (Figure S2) suggests a direct relationship between the sorption capacity of CO_2 versus the ultramicropore volumes of the honeycomb-like N-doped ultramicroporous biochar, which is consistent with the previous literature based on machine learning [67]. Besides, the comparison of sorption performance among the samples versus previously reported biochar is summarized and tabulated in Table 2, in which the PNdCA outperforms previously reported biochar, trapping the highest amount of CO_2 molecules at 298 K and 1 bar. Additionally, PNdCA demonstrates efficiently CO_2 encapsulation of 5.45 mmol/g at 273 K and 1 bar (Figure S3) outperforming DNdCA (4.19 mmol/g) and HNdCA (3.94 mmol/g) under the same condition. The sorption heat, calculated via these isotherms at 273 K and 298 K (Figure 4b), serves as an indicator of affinity between sorbents and CO_2 molecules. For PNdCA, DNdCA, and HNdCA, the average sorption heat is approximately 23 kJ/mol, characteristic of physisorption behaviors. This process transitions from single-layer sorption of CO_2 to multi-layer sorption, leading to an initially stronger affinity for CO_2 molecules and consequently higher sorption heat at low sorption capacities. Despite the maximum sorption heat exceeding 35 kJ/mol, it still remains within the typical physisorption range [68].

Table 2: The comparison of the sorption performance between honeycomb-like N-doped ultramicroporous biochar versus previously reported biochar

Materials	Precursors	Sorption capacity [mmol/g]	Temperature [K]	Pressure [bar]	Ref.
HNdCA	Corncob	3.19	298	1	This work
DNdCA	Corncob	3.56	298	1	This work
PNdCA	Corncob	4.15	298	1	This work

PNdCA	Corncob	5.45	273	1	This work
SG-CN(2)	Sugarcane bagasse	3.34	298	1	[38]
HAC-850-KOH	Walnut shell	3.08	298	1	[39]
WSM-550-3	Water caltrop shell	4.06	298	1	[40]
LCM-550-2	Lotus leaf	3.87	298	1	[41]
NAC-800-3	Corncob	2.81	298	1	[69]
AC-TBG	Tasmanian Blue Gum tree bark	3.20	298	1	[70]
NC700	Tobacco stem	3.70	298	1	[71]
MPC-1	Tobacco stem	3.30	298	1	[72]
CPU800	Corncob	3.80	298	1	[73]

The sorption isotherms of activated samples at 298 K have been fitted using various models, including Langmuir, Freundlich, Toth, Sips, and Temkin, and their detailed fitting results are presented in Table S1 and Figure 4c-4e. The Freundlich model emerges as an excellent empirical formula, exhibiting high regression correlation coefficients of all the activated honeycomb-like N-doped ultramicroporous biochar. The fitting parameters (n) consistently remain above 2, indicating a rapid increase in sorption capacity at relatively low pressures for the activated biochar. However, the Temkin model, which is more suitable for the chemisorption processes [74], does not perform well in accurately reconstructing the sorption isotherms of samples, as indicated by the large errors in low-pressure areas. While the Langmuir models exhibit high regression correlation coefficients over 0.9865, they show a poor fitting effect at 1 bar. On the positive side, the Toth models and Sips models, which are modifications of the Langmuir models concerning surface heterogeneity, provide excellent predictions with high regression correlation coefficients. The parameter representing surface heterogeneity (n) in these models aligns with the degree of defects determined by the Raman spectroscopy. In particular, the Sips model exhibits more accurate fitting behaviors at relative low pressure (Figure 4c-4e). The regression correlation coefficients of Sips models reach 0.9942, indicating superior fitting accuracy. The maximum sorption capacity (q_m) of PNdCA in this model reaches 5.45 mmol/g, surpassing that of DNdCA and HNdCA by approximately 16.7% and 23.0%, respectively.

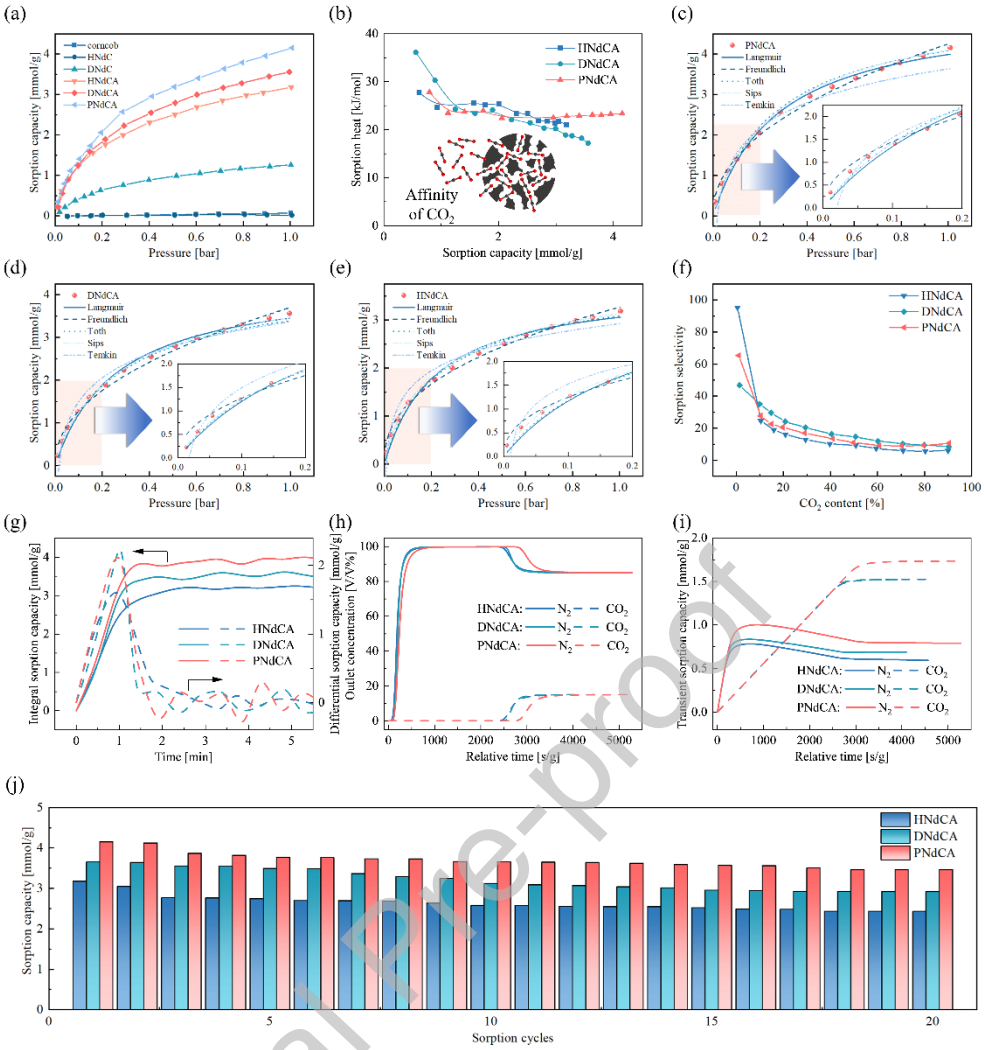

Figure 4. Sorption performance for CO_2: (a) experiments isothermals of samples at 298 K, (b) sorption heat, (c) reconstructed isothermal of PNdCA, (d) reconstructed isothermal of DNdCA, (e) reconstructed isothermal of HNdCA, (f) sorption selectivity of samples at 298 K and 1 bar, (g) sorption kinetics, (h) outlet concentration breakthrough curve, (i) transient sorption capacity curve, (j) cyclic robustness of samples trapping CO_2 at 298 K for 20 vacuum pressure swing cycles.

The sorption selectivity of CO_2 in the gas mixture balanced with N_2 at 1 bar and 298 K (Figure 4f) is evaluated using the ideal adsorption solution theory. The N_2 sorption capacity is determined from N_2 sorption isotherms at 298 K (Figure S4) with a maximum sorption capacity below 0.5 mmol/g. Among all the honeycomb-like N-doped ultramicroporous biochar, DNdCA exhibits the maximum sorption selectivity (24.06-35.12), followed by PNdCA (20.57-27.59) and HNdCA (16.06-24.54) under post-combustion conditions with varying CO_2 concentrations (typically ranging from 20% to 10%). Despite N_2 and CO_2 having similar molecular diameters (3.64 Å for N_2 and 3.3 Å for CO_2), the nonpolar linear structure of CO_2, combined with its strong affinity for the sorption sites that accept or donate electrons, contributes to enhanced sorption selectivity. CO_2 exhibits strong $\pi_{3\text{-}4}$ dislocated bonds

involving electrons from the *p* orbital of both carbon and oxygen, with the remaining electrons from the oxygen's *p* orbital contributing to the anti-bond orbital of CO_2 [75]. Moreover, there is a stronger correlation between sorption selectivity and the surface nitrogen content rather than the bulk nitrogen content of the honeycomb-like N-doped ultramicroporous biochar, as evident from Figure 4f, XPS survey scans (Figure 3d), and EA (Figure S1). This suggests that the variations in sorption capacities can be attributed to the greater polarizability and quadrupole moment of the CO_2 molecule compared to N_2. Consequently, CO_2 molecules tend to preferentially sorb onto the surfaces of the samples with heterogeneous electric fields, facilitated by the presence of nitrogen doping in the biochar.

Figure 4g highlights the sorption kinetics of the honeycomb-like N-doped ultramicroporous biochar. Among the samples, DNdCA and PNdCA demonstrate outstanding sorption kinetics, achieving peak differential sorption capacity within the initial two minutes, with maxima of approximately 2.2 mmol/g and 2.1 mmol/g, respectively. However, DNdCA experiences a pronounced attenuation in differential sorption capacity between the first and the second seconds. Consequently, the integral sorption capacity of DNdCA reaches 3.40 mmol/g within these two minutes, equivalent to 86.1% of the integral sorption capacity of PNdCA (3.95 mmol/g). Notably, both samples achieve 95% of their total sorption capacity within this brief initial period, underscoring their rapid and efficient CO_2 sorption performance.

The dynamic breakthrough experiments (Figure 4h and Figure 4i) further validate the reliability of the sorption capacity and selectivity observed in the static tests for honeycomb-like N-doped ultramicroporous biochar. Initially, N_2 rapidly traverse through the sorbents, exiting the outlet between 271.3 s/g ~ 337.7 s/g. In contrast, CO_2 remains undetected at the outlet during the early stages as it is swiftly captured within the ultramicropores of samples. For HNdCA and DNdCA, the breakthrough points for CO_2 are recorded at 2500.9 s/g to 2571.1 s/g, with the half-dry points at 2680.5 s/g to 2681.7 s/g and the dry point at 3189.2 s/g to 3038.0 s/g. While PNdCA exhibits superior performance with delayed breakthrough, half-dry, and dry points occurring at 2851.9 s/g, 3046.7 s/g, and 3577.9 s/g, respectively. The transient sorption capacity curve (Figure 4i) indicates that all samples initially favor N_2 sorption. However, as CO_2 flow continues, a competitive sorption process ensues, with CO_2 molecules snatching the sorption sites of N_2, leading to increased CO_2 sorption capacity and reduced N_2 sorption capacity. Dynamic test results reveal CO_2 sorption capacities of approximately 1.52 mmol/g for HNdCA and DNdCA, and 1.73 mmol/g for PNdCA, with deviations ranging from 0.03% to 4.29% compared to static test results under similar conditions. These findings confirm that PNdCA demonstrates the best dynamic sorption and separation performance among the samples.

Figure 4j demonstrates the cyclic robustness of the honeycomb-like N-doped ultramicroporous biochar, tested at 298 K for 20 vacuum pressure swing cycles. The average sorption capacities of HNdCA, DNdCA, and PNdCA are observed to be 2.52 mmol/g, 2.96 mmol/g, and 3.57 mmol/g, respectively, with attenuation rates of approximately 20.75%, 20.22%, and 13.98% compared to the sorption capacities

shown in Figure 4a. Notably, the observed performance degradation is mainly concentrated in the first ten cycles, with the degradation amplitude of PNdCA being less than 5% in the subsequent cycles. This suggests that PNdCA exhibits a higher degree of stability and reversibility, particularly after the initial cycles, manifesting its robustness and suitability for repeated selective carbon capture process and offering promising prospects for their application as sorption materials.

By modeling the honeycomb-like N-doped ultramicroporous biochar as a graphene layer cluster, the impact of N doping on CO_2 sorption characteristics is analyzed comprehensively. In Figure 5a, the visualizations of the electrostatic potential distribution reveal that while the atomic arrangement and bonding modes of the cluster remain similar before and after N doping, the doping significantly alters the electrostatic potential gradient. Before N doping, the potential distribution is relatively uniform, with a local gradient ranging from 0 Ha/Å to 0.0091 Ha/Å, while the electrostatic potential at the doping site shifts substantially after doping, increasing the gradient to -0.0669 Ha/Å to -0.0507 Ha/Å. Regarding sorption structure, undoped clusters sorb CO_2 molecules centrally, whereas N-doped clusters demonstrate CO_2 sorption directly oriented to the N doping sites. The shortest distance between the CO_2 molecule and the doping site decreased to 3.11 Å (Figure 5b), approximately 95.99% of the pre-doping distance, indicating enhanced affinity. This underscores N doping's critical role in facilitating efficient CO_2 capture processes.

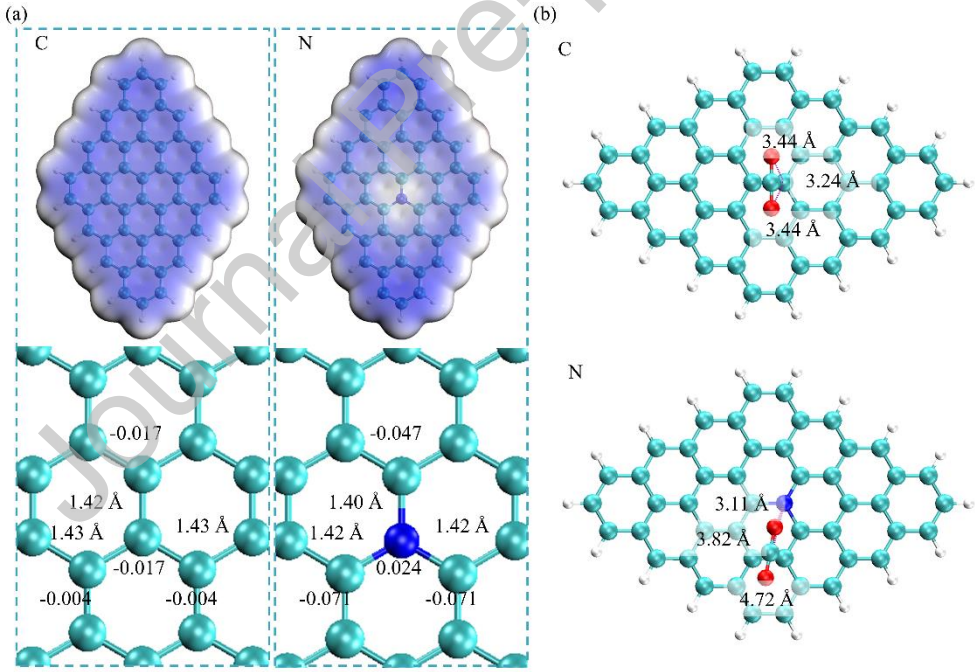

Figure 5. DFT analysis of honeycomb-like N-doped ultramicroporous biochar: (a) electrostatic potential distribution and charge distribution, (b) microstructural modifications of the cluster upon CO_2 sorption.

4. Conclusion

In this study, the straightforward one-pot carbonization-activation synthesis is established as the optimal approach for synthesizing honeycomb-like N-doped ultramicroporous carbons derived from biomass for CO_2 capture using urea as a nitridation agent and KOH as a porogen. The resulting materials exhibit densely packed ultramicropores arranged in a honeycomb-like pattern, abundant functional groups, and graphitic carbon with sufficient defects, contributing to exceptional CO_2 sorption performance. The honeycomb-like N-doped ultramicroporous biochar exhibits exceptional CO_2 sorption capacities, reaching up to 4.15 mmol/g (at 1 bar and 298 K) and 5.45 mmol/g (at 1 bar and 273 K), with sorption heat fluctuating around 23 kJ/mol, indicative of physisorption. Sorption selectivity between CO_2 and N_2 is significantly influenced by the surface nitrogen content of the materials. Moreover, the biochar demonstrates outstanding durability, with an attenuation rate as low as approximately 13.98% over 20 vacuum pressure swing cycles, underscoring its robustness and suitability for repeated CO_2 capture processes. These findings highlight the potential of honeycomb-like N-doped ultramicroporous biochar synthesized through a simplified one-pot carbonization-activation method as promising candidates for CO_2 capture applications. Their superior sorption performance, coupled with the practical viability of their synthesis, suggests a substantial leap forward in advancing accessible and efficient carbon capture technologies.

CRedit authorship contribution statement

Chen Zhang: Investigation, Methodology, Writing - Original Draft, Visualization, Formal analysis. **Duoyong Zhang:** Methodology, Writing - Review & Editing, Validation. **Xinqi Zhang:** Methodology, Writing - Review & Editing. **Linrui Chen:** Visualization. **Xiaoou Chen:** Visualization. **Yongqiang Tian**: Writing - Review & Editing. **Liwei Wang:** Conceptualization, Resources, Writing - Review & Editing, Supervision, Project administration.

Declaration of competing interest

All the authors declare that they have no conflicts of interest in this work.

Acknowledgments

This work was supported by grants from the National Natural Science Foundation of China (Grant No.523B2057 and No.52236004) and the non-carbon energy conversion and utilization institute under the Shanghai Class IV Peak Disciplinary Development Program.

References

[1] O. Hoegh-Guldberg, D. Jacob, M. Taylor, et al., The human imperative of stabilizing global climate change at 1.5^{o}C, Science 365(6459) (2019) 1263.

[2] T. Al-Attas, S. K. Nabil, A. S. Zeraati, et al., Permselective MOF-based gas diffusion electrode for direct conversion of CO_2 from quasi flue gas, ACS Energy Lett. 8(1) (2023) 107-115.
[3] R. Sahoo, S. Mondal, D. Mukherjee, et al., Metal-organic frameworks for CO_2 separation from flue and biogas mixtures, Adv. Funct. Mater. 32(45) (2022) 2207197.
[4] C. Hou, D. R. Kumar, Y. Jin, et al., Porosity and hydrophilicity modulated quaternary ammonium-based sorbents for CO_2 capture, Chem. Eng. J. 413 (2021) 127532.
[5] H. Lyu, O. I. F. Chen, N. Hanikel, et al., Carbon dioxide capture chemistry of amino acid functionalized metal-organic frameworks in humid flue gas, J. Am. Chem. Soc. 144(5) (2022) 2387-2396.
[6] S. G. Subraveti, S. Roussanaly, R. Anantharaman, et al., How much can novel solid sorbents reduce the cost of post-combustion CO_2 capture? A techno-economic investigation on the cost limits of pressure-vacuum swing adsorption, Appl. Energy 306 (2022) 117955.
[7] S. Ullah, K. Tan, D. Sensharma, et al., CO_2 capture by hybrid ultramicroporous TIFSIX-3-Ni under humid conditions using non-equilibrium cycling, Angew. Chem. Int. Ed. 61(35) (2022) e202206613.
[8] S. Ni, N. Wang, X. Guo, et al., Li_4SiO_4-based sorbents from expanded perlite for high-temperature CO_2 capture, Chem. Eng. J. 410 (2021) 128357.
[9] G. Tan, X. Hu, C. Wang, et al., High efficiency CO_2 sorption property of Li_4SiO_4 sorbent pebbles via a simple rolling ball method, Sep. Purif. Technol. 298 (2022) 121662.
[10] K. Wang, F. Gu, P. T. Clough, et al., Molten shell-activated, high-performance, un-doped Li_4SiO_4 for high-temperature CO_2 capture at low CO_2 concentrations, Chem. Eng. J. 408 (2021) 127353.
[11] W. Gao, J. Xiao, Q. Wang, et al., Unravelling the mechanism of intermediate-temperature CO_2 interaction with molten-$NaNO_3$-salt-promoted MgO, Adv. Mater. 34(4) (2022) 2106677.
[12] H. J. Yoon, C. H. Lee, K. B. Lee, Mass transfer enhanced CaO pellets for CO_2 sorption: Utilization of CO_2 emitted from $CaCO_3$ pellets during calcination, Chem. Eng. J. 421 (2021) 129584.
[13] R. Chang, X. Wu, O. Cheung, et al., Synthetic solid oxide sorbents for CO_2 capture: State-of-the art and future perspectives, J. Mater. Chem. A 10(4) (2022) 1682-1705.
[14] M. E. Zick, S. M. Pugh, J. H. Lee, et al., Carbon dioxide capture at nucleophilic hydroxide sites in oxidation-resistant cyclodextrin-based metal-organic frameworks, Angew. Chem. Int. Ed. 61(30) (2022) e202206718.
[15] M. Cavallo, C. Atzori, M. Signorile, et al., Cooperative CO_2 adsorption mechanism in a perfluorinated CeIV-based metal organic framework, J. Mater. Chem. A 11(11) (2023) 5568-5583.
[16] M. Breunig, M. Dorner, J. Senker, Ultramicroporous polyimides with hierarchical morphology for carbon dioxide separation, J. Mater. Chem. A 9(21) (2021) 12797-12806.

[17] M. Åhlén, A. Jaworski, M. Strømme, et al., Selective adsorption of CO_2 and SF6 on mixed-linker ZIF-7-8s: The effect of linker substitution on uptake capacity and kinetics, Chem. Eng. J. 422 (2021) 130117.
[18] C. Zhang, X. Zhang, T. Su, et al., Modification schemes of efficient sorbents for trace CO_2 capture, Renewable Sustainable Energy Rev. 184 (2023) 113473.
[19] M. Sharma, M. A. Snyder, Facile synthesis of flower-like carbon microspheres for carbon dioxide capture, Microporous Mesoporous Mater. 335 (2022) 111801.
[20] J. Shao, J. Wang, Q. Yu, et al., Unlocking the potential of N-doped porous carbon: Facile synthesis and superior CO_2 adsorption performance, Sep. Purif. Technol. 333 (2024) 125891.
[21] D. L. Fu, Y. Park, M. E. Davis, Zinc containing small-pore zeolites for capture of low concentration carbon dioxide, Angew. Chem. Int. Ed. 61(5) (2022) e202112916.
[22] C. Zhang, D. Zhang, X. Zhang, et al., Rubik's cube-shaped Linde type A zeolite synthesized from biomass for carbon dioxide capture, Cell Rep. Phys. Sci. 5(4) (2024) 101889.
[23] F. Zhang, H. Shang, L. Wang, et al., Construction of a porous metal-organic framework with a high density of open Cr sites for record N_2/O_2 separation, Adv. Mater. 33(37) (2021) 2100866.
[24] C. Zhang, T. Su, X. Zhang, et al., Porous core-membrane microstructured nanomaterial composed of deep eutectic solvents and MOF-808 for CO_2 capture, ChemSusChem 16(24) (2023) e202300864.
[25] K. Wang, Y. Tang, Q. Jiang, et al., A thiophene-containing covalent triazine-based framework with ultramicropore for CO_2 capture, J. Energy Chem. 26(5) (2017) 902-908.
[26] X. Zhu, M. Lyu, T. Ge, et al., Modified layered double hydroxides for efficient and reversible carbon dioxide capture from air, Cell Rep. Phys. Sci. 2(7) (2021) 100484.
[27] L. Liu, S. Jin, Y. Park, et al., Sorption equilibria, kinetics, and temperature-swing adsorption performance of polyethyleneimine-impregnated silica for post-combustion carbon dioxide capture, Sep. Purif. Technol. 266 (2021) 118582.
[28] G. L. Seah, L. Y. Wang, L. F. Tan, et al., Ordered mesoporous alumina with tunable morphologies and pore sizes for CO_2 capture and dye separation, ACS Appl. Mater. Interfaces 13(30) (2021) 36117-36129.
[29] S. Qadir, H. Su, D. Li, et al., Low-cost preferential different amine grafted silica spheres adsorbents for DAC CO_2 removal, J. Energy Chem. 75 (2022) 494-503.
[30] M. Bilal, J. Li, H. Guo, et al., High-voltage supercapacitive swing adsorption of carbon dioxide, Small 19(24) (2023) 2207834.
[31] P. H. Ho, V. Lofty, A. Basta, et al., Designing microporous activated carbons from biomass for carbon dioxide adsorption at ambient temperature. A comparison between bagasse and rice by-products, J. Cleaner Prod. 294 (2021) 126260.
[32] L. Cao, X. Zhang, Y. Xu, et al., Straw and wood based biochar for CO_2 capture: Adsorption performance and governing mechanisms, Sep. Purif. Technol. 287 (2022) 120592.
[33] S. Khodabakhshi, S. Kiani, Y. Niu, et al., Facile and environmentally friendly

synthesis of ultramicroporous carbon spheres: A significant improvement in CVD method, Carbon 171 (2021) 426-436.
[34] Y. Shen, Preparation of renewable porous carbons for CO_2 capture - A review, Fuel Process. Technol. 236 (2022) 107437.
[35] Y. Li, J. Wang, S. Fan, et al., Nitrogen-doped hierarchically porous carbon spheres for low concentration CO_2 capture, J. Energy Chem. 53 (2021) 168-174.
[36] D. Wei, X. Ma, T. Yang, et al., N-doping porous carbon with rich narrow micropores for highly efficient CO_2 selective adsorption: Insight from experimental and theoretical study, Appl. Surf. Sci. 605 (2022) 154777.
[37] C. Zhang, Y. Zhang, T. Su, et al., Molecular simulation on carbon dioxide capture performance for carbons doped with various elements, Energy Storage Sav. 2(2) (2023) 435-441.
[38] S.O. Adio, S.A. Ganiyu, M. Usman, et al., Facile and efficient nitrogen modified porous carbon derived from sugarcane bagasse for CO_2 capture: Experimental and DFT investigation of nitrogen atoms on carbon frameworks, Chem. Eng. J. 382 (2020) 122964.
[39] Y. Xu, Z. Yang, G. Zhang, et al., Excellent CO_2 adsorption performance of nitrogen-doped waste biocarbon prepared with different activators, J. Cleaner Prod. 264 (2020) 121645.
[40] Z. Zhao, C. Ma, F. Chen, et al., Water caltrop shell-derived nitrogen-doped porous carbons with high CO_2 adsorption capacity, Biomass Bioenergy 145 (2021) 105969.
[41] Q. Li, S. Liu, L. Wang, et al., Efficient nitrogen doped porous carbonaceous CO_2 adsorbents based on lotus leaf, J. Environ. Sci. 103 (2021) 268-278.
[42] L. Yue, L. Rao, L. Wang, et al., Efficient CO_2 capture by nitrogen-doped biocarbons derived from rotten strawberries, Ind. Eng. Chem. Res. 56(47) (2017) 14115-14122.
[43] L. Rao, R. Ma, S. Liu, et al., Nitrogen enriched porous carbons from d-glucose with excellent CO_2 capture performance, Chem. Eng. J. 362 (2019) 794-801.
[44] X. Wang, W. Zeng, C. Xin, et al., The development of activated carbon from corncob for CO_2 capture, RSC Adv. 12(51) (2022) 33069-33078.
[45] C. Liu, Y. Zhi, Q. Yu, et al., Sulfur-enriched nanoporous carbon: A novel approach to CO_2 adsorption, ACS Appl. Nano Mater. 7(5) (2024) 5434-5441.
[46] M. J. Frisch, G. W. Trucks, H. B. Schlegel, et al., Gaussian 16 Rev. C.01, Wallingford, CT, 2016.
[47] A.D. Becke, Density‐functional thermochemistry. III. The role of exact exchange, J. Chem. Phys. 98(7) (1993) 5648-5652.
[48] Y. Zhao, D.G. Truhlar, The M06 suite of density functionals for main group thermochemistry, thermochemical kinetics, noncovalent interactions, excited states, and transition elements: two new functionals and systematic testing of four M06-class functionals and 12 other functionals, Theor. Chem. Acc. 120(1) (2008) 215-241.
[49] F. Weigend, Accurate coulomb-fitting basis sets for H to Rn, Phys. Chem. Chem. Phys. 8(9) (2006) 1057-1065.
[50] F. Weigend, R. Ahlrichs, Balanced basis sets of split valence, triple zeta valence

and quadruple zeta valence quality for H to Rn: Design and assessment of accuracy, Phys. Chem. Chem. Phys. 7(18) (2005) 3297-3305.
[51] S. Grimme, J. Antony, S. Ehrlich, et al., A consistent and accurate ab initio parametrization of density functional dispersion correction (DFT-D) for the 94 elements H-Pu, J. Chem. Phys. 132(15) (2010).
[52] W. Humphrey, A. Dalke, K. Schulten, VMD: Visual molecular dynamics, J. Mol. Graph. 14(1) (1996) 33-38.
[53] T. Lu, F. Chen, Multiwfn: A multifunctional wavefunction analyzer, J. Comput. Chem. 33(5) (2012) 580-592.
[54] D. Feng, P. Yan, Y. Li, et al., Mechanism of functionalized biochar/K_2CO_3 cross-linking capture of multi-concentration CO_2, Fuel Process. Technol. 241 (2023) 107614.
[55] C. Pan, S. Zhang, Y. Fan, et al., Bioconversion of corncob to hydrogen using anaerobic mixed microflora, Int. J. Hydrogen Energy 35(7) (2010) 2663-2669.
[56] Q. Xia, C. Chen, Y. Yao, et al., In *situ* lignin modification toward photonic wood, Adv. Mater. 33(8) (2021) 2001588.
[57] B. Zhang, L. Wang, C. Zhang, et al., High-performance cellulose nanofiber-derived composite films for efficient thermal management of flexible electronic devices, Chem. Eng. J. 439 (2022) 135675.
[58] Z. Xu, X. Zhang, X. Yang, et al., Synthesis of Fe/N co-doped porous carbon spheres derived from corncob for supercapacitors with high performances, Energy Fuels 35(17) (2021) 14157-14168.
[59] R. Xue, W. Xu, X. Ma, et al., Targeted enhancement of ultra-micropore in highly oxygen-doped carbon derived from biomass for efficient CO_2 capture: Insights from experimental and molecular simulation studies, Sep. Purif. Technol. 353 (2025) 128472.
[60] Z. Li, L. Deng, I.A. Kinloch, et al., Raman spectroscopy of carbon materials and their composites: Graphene, nanotubes and fibres, Prog. Mater Sci. 135 (2023) 101089.
[61] J. Bai, J. Shao, Q. Yu, et al., Sulfur-doped porous carbon adsorbent: A promising solution for effective and selective CO_2 capture, Chem. Eng. J. 479 (2024) 147667.
[62] J. Yu, M. Guo, F. Muhammad, et al., One-pot synthesis of highly ordered nitrogen-containing mesoporous carbon with resorcinol-urea-formaldehyde resin for CO_2 capture, Carbon 69 (2014) 502-514.
[63] Q. Shi, Y. Wang, Z. Wang, et al., Three-dimensional (3D) interconnected networks fabricated via in-situ growth of N-doped graphene/carbon nanotubes on Co-containing carbon nanofibers for enhanced oxygen reduction, Nano Res. 9(2) (2016) 317-328.
[64] M. Chen, Z. Yan, J. Luan, et al., π-π electron-donor-acceptor (EDA) interaction enhancing adsorption of tetracycline on 3D PPY/CMC aerogels, Chem. Eng. J. 454 (2023) 140300.
[65] J. Niu, C. Chokradjaroen, N. Saito, Graphitic N-doped graphene via solution plasma with a single dielectric barrier, Carbon 199 (2022) 347-356.
[66] L. Torrisi, L. Silipigni, M. Cutroneo, et al., Graphene oxide as a radiation

sensitive material for XPS dosimetry, Vacuum 173 (2020) 109175.
[67] X. Ma, W. Xu, R. Su, et al., Insights into CO_2 capture in porous carbons from machine learning, experiments and molecular simulation, Sep. Purif. Technol. 306 (2023) 122521.
[68] L. Tian, Y. Zhi, Q. Yu, et al., Enhanced CO_2 adsorption capacity in highly porous carbon materials derived from melamine-formaldehyde resin, Energy Fuels 38(14) (2024) 13186-13195.
[69] Z. Geng, Q. Xiao, H. Lv, et al., One-step synthesis of microporous carbon monoliths derived from biomass with high nitrogen doping content for highly selective CO_2 capture, Sci. Rep. 6(1) (2016) 30049.
[70] T. Prasankumar, D. Salpekar, S. Bhattacharyya, et al., Biomass derived hierarchical porous carbon for supercapacitor application and dilute stream CO_2 capture, Carbon 199 (2022) 249-257.
[71] X. Ma, C. Su, B. Liu, et al., Heteroatom-doped porous carbons exhibit superior CO_2 capture and CO_2/N_2 selectivity: Understanding the contribution of functional groups and pore structure, Sep. Purif. Technol. 259 (2021) 118065.
[72] X. Ma, Y. Wu, M. Fang, et al., In-situ activated ultramicroporous carbon materials derived from waste biomass for CO_2 capture and benzene adsorption, Biomass Bioenergy 158 (2022) 106353.
[73] H. Li, M. Tang, X. Huang, et al., An efficient biochar adsorbent for CO_2 capture: Combined experimental and theoretical study on the promotion mechanism of N-doping, Chem. Eng. J. 466 (2023) 143095.
[74] C. S. T. Araújo, I. L. S. Almeida, H. C. Rezende, et al., Elucidation of mechanism involved in adsorption of Pb(II) onto lobeira fruit (Solanum lycocarpum) using Langmuir, Freundlich and Temkin isotherms, Microchem. J. 137 (2018) 348-354.
[75] J. Liu, Y. Wei, Y. Zhao, Trace carbon dioxide capture by metal-organic frameworks, ACS Sustainable Chem. Eng. 7(1) (2019) 82-93.

Profile + Photo + BRID

Chen Zhang is a Ph.D. candidate in the Institute of Refrigeration and Cryogenics, Shanghai Jiao Tong University. He undertook the first NSFC projects of basic research program for young students in 2024. His research focuses on the development of advanced sorption materials and thermodynamic cycle construction for carbon dioxide capture. BRID: 07763.00.79868

Liwei Wang* is a professor at the Institute of Refrigeration and Cryogenics, School of Mechanical Engineering, Shanghai Jiao Tong University. As the international incoming fellow, she worked in Warwick University in 2009 and Newcastle University in 2010. Her research focuses on materials, cycles, and systems for sorption technology. BRID: 09211.00.00607

Graphical Abstract

The honeycomb-like nitrogen-doped ultramicroporous biochar developed through the one-pot carbonization-activation synthesis method is preferred as a promising sorption material for CO_2 capture since the it predominantly exists in a graphite state of carbon with sufficient defects, abundant functional groups, high surface and bulk nitrogen content, and a large number of CO_2 sorption sites.

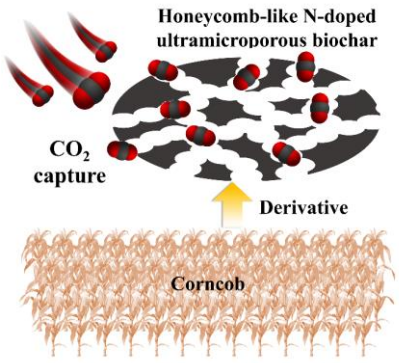

Declaration of interests

☒ The authors declare that they have no known competing financial interests or personal relationships that could have appeared to influence the work reported in this paper.

☐The authors declare the following financial interests/personal relationships which may be considered as potential competing interests: